

INFALLING FAINT [O II] EMITTERS IN ABELL 851. I. SPECTROSCOPIC CONFIRMATION OF NARROWBAND-SELECTED OBJECTS

TARO SATO¹ AND CRYSTAL L. MARTIN^{2,3,4}

Department of Physics, University of California, Santa Barbara, CA 93106-9530, U.S.A.

To appear in Astrophysical Journal

ABSTRACT

We report on a spectroscopic confirmation of narrowband-selected [O II] emitters in Abell 851 catalogued by Martin et al. (2000). The optical spectra obtained from the Keck I Low Resolution Imaging Spectrometer (LRIS) and Keck II Deep Imaging Multi-Object Spectrograph (DEIMOS) have confirmed [O II] λ 3727 emission in narrowband-selected cluster [O II] candidates at a $\approx 85\%$ success rate for faint ($i \lesssim 25$) blue ($g-i < 1$) galaxies. The rate for the successful detection of [O II] emission is a strong function of galaxy color, generally proving the efficacy of narrowband [O II] search supplemented with broadband colors in selecting faint cluster galaxies with recent star formation. Balmer decrement-derived reddening measurements show a high degree of reddening [$E(B-V) \gtrsim 0.5$] in a significant fraction of this population. Even after correcting for dust extinction, the [O II]/H α line flux ratio for the high- $E(B-V)$ galaxies remains generally lower by a factor of ~ 2 than the mean [O II]/H α ratios reported by the studies of nearby galaxies. The strength of [O II] equivalent width shows a negative trend with galaxy luminosity while the H α equivalent width does not appear to depend as strongly on luminosity. This in part is due to the high amount of reddening observed in luminous galaxies. Furthermore, emission line ratio diagnostics show that AGN-like galaxies are abundant in the high luminosity end of the cluster [O II]-emitting sample, with only moderately strong [O II] equivalent widths, consistent with a scenario of galaxy evolution connecting AGNs and suppression of star-forming activity in massive galaxies.

Subject headings: galaxy cluster: general — galaxies: clusters: individual (Abell 851; Cl0939+4713) — galaxies: dwarf — galaxies: evolution — galaxies: starburst — cosmology: observations

1. INTRODUCTION

The currently popular cosmological paradigm predicts that galaxy clusters, which are the largest gravitationally bound systems, evolve by merging and accreting smaller structures from the surrounding field region (Kauffmann 1995a,b). Results from recent simulations have shown that galaxy clusters in Λ CDM cosmology have two rather distinct phases in their mass assembly history, merger-dominated and accretion-dominated phases (Zhao et al. 2003). While the star-forming activities in the universe are generally declining since $z \sim 2$ (Lilly et al. 1996; Madau et al. 1996), some galaxy clusters may remain dynamically active at intermediate redshifts of $z \sim 0.5$ (Tasitsiomi et al. 2004), potentially triggering cluster-scale enhancement of star-forming activity. The dynamic range in local environments that galaxy clusters offer has been an essential aid for the study of galaxy evolution, particularly of star-forming field spirals into passively-evolving cluster spheroidal galaxies, spanning a wide range of morphological types in the Hubble sequence.

As the connection between structure formation and galaxy clusters becomes clearer, most recent efforts in cluster galaxy surveys have focused on wide-field imaging in an attempt to trace the substructures extending from their central regions out to larger cluster radii, where galaxies are not yet virialized within strong cluster gravitational potentials (Abraham et al. 1996; Kodama et al. 2005). Such recent studies have shown that the mechanism responsible for the transformation of cluster galaxies must be in effect well beyond the cluster virial radius, well before the galaxies at infall reach the central re-

gion of a cluster (e.g., Balogh et al. 1997; Treu et al. 2003; Moran et al. 2005).

Martin et al. (2000, hereafter MLF00) used narrowband and broadband photometry to select faint [O II] λ 3727 emission-line candidates in a rich, moderately distant ($z \simeq 0.4069$) galaxy cluster Abell 851 (Cl0939+4713; $9^{\text{h}}42^{\text{m}}56^{\text{s}}.2, 46^{\circ}59'12''.0$). The cluster offers an especially interesting laboratory for the study of cluster galaxy evolution, because there is observational evidence of large-scale filaments detected via photometric redshift technique by Kodama et al. (2001), giving observers a snapshot of the on-going assembly of the cluster. Even before the identification of the filaments, Abell 851 had drawn attention due to its high fraction of blue and post-starburst galaxy population (Dressler et al. 1999) compared to other clusters at similar redshifts (Lotz et al. 2003). These observations are apparently related to the X-ray observations indicating highly dynamically active state of Abell 851 (Schindler & Wambsganss 1996; Schindler et al. 1998; De Filippis et al. 2003).

MLF00 narrowband search yielded 371 cluster emission-line member candidates over the projected area of $\sim 181 \text{ arcmin}^2 \approx 4.4 \text{ Mpc} \times 4.4 \text{ Mpc}$ at the cluster redshift. The completeness limit of the narrowband survey was $m_{5129}(\text{AB}) \simeq 24$ for galaxies with [O II] emission equivalent width of $\lesssim -11 \text{ \AA}$, making it among the faintest surveys of the kind at $z \sim 0.4$. The locus in the $(g-i)$ - i color-magnitude diagram and their small isophotal area suggested that a significant number of the [O II] emission candidates were dwarf galaxies. Dwarf and large spiral galaxies are expected to respond differently to cluster tidal fields due to their different mass concentrations (Moore et al. 1999). The efforts spanning a few decades have established such empirical relations as the morphology-density relation (Dressler 1980) and the Butcher-Oemler effect (Butcher & Oemler

¹ taro@physics.ucsb.edu

² cmartin@physics.ucsb.edu

³ Packard Fellow

⁴ Alfred P. Sloan Foundation Fellow

1984) for the bright, giant cluster galaxies, but the underlying physical processes that are responsible for the evolution of galaxy properties and therefore the aforementioned empirical relations have yet to be well constrained. The sign of the differential evolution between dwarf and giant galaxies is even more obscure, since few wide-field surveys to date have sampled faint galaxies at high redshifts.

As a spectroscopic follow-up of MLF00, we have obtained an extensive set of spectra of the [O II]-emitting candidates using the Keck I Low Resolution Imaging Spectrometer (LRIS; Oke et al. 1995) and Keck II Deep Imaging Multi-Object Spectrograph (DEIMOS; Faber et al. 2003). In a series of papers drawing on this spectroscopic sample, we wish to study infalling faint star-forming galaxies in a highly dynamically active galaxy cluster at intermediate redshift. We present the observation, data reduction, and various measurement methods employed in this study in § 2.

Although galaxy clusters are well localized within redshift space and much denser in their projected galaxy number density compared to that of the surrounding field, an inherent observational challenge in wide-field study of clusters is to obtain secure membership identification of cluster galaxies. Various photometric methods exist for this purpose, each sensitive to different spectral features of distant objects. Narrowband photometry is a useful method of selecting emission-line objects within a wide field of view over a redshift range defined by the filter bandpass. While efficient for cluster galaxy surveys, narrowband selected objects always need further constraints on their true identity via other means, since the selection method is prone to detecting emission lines or prominent spectral breaks from foreground or background objects at different redshifts. Therefore in § 3 we assess the efficacy of narrowband technique in our narrowband-selected sample of galaxies. In the same section we also explore possible systematic errors introduced by using two independent sets of measurements, narrowband photometry and spectroscopy.

Studies of intermediate redshift galaxies often use [O II] λ 3727 emission line as a tracer of star-forming activity for its availability within the optical wavelengths out to $z \sim 1$. The justification for the use of the [O II] emission line as a star formation tracer originates from the apparent empirical correlation found between [O II] λ 3727 flux and H α recombination line flux within the sample of galaxies with various morphological types in the local universe (Gallagher, Hunter, & Bushouse 1989; Kennicutt 1992). Low-order Balmer recombination lines are presumed to be good star formation indicators because of their tight coupling to the UV radiation intensity from young O- and B-type stars in H II regions. The correlation between the [O II] and the Balmer recombination lines, however, is complicated by its dependence on the elemental abundances and ionization state of the parent H II region. The [O II] λ 3727, being on the bluest side of optical wavelengths, also suffers greater dust extinction. As dust reprocessing of starlight appears to be more important in high redshift galaxies (e.g., Hicks et al. 2002; Le Floch et al. 2005), the reliability of the [O II] emission as a star formation tracer, especially for high redshift galaxies, still remains an open topic (Jansen et al. 2001). For this reason, we study in § 4 the properties of [O II] emitters as observed in our sample. We then summarize our findings in § 5.

Throughout this paper, we use the standard Λ CDM cosmology, $(\Omega_m, \Omega_\Lambda) = (0.3, 0.7)$, with $H_0 = 70 \text{ km s}^{-1} \text{ Mpc}^{-1}$. At the

distance of Abell 851 ($z = 0.4069$), $1''$ on the sky corresponds to a projected physical distance of 5.43 kpc, and the lookback time to the galaxy cluster is 4.3 Gyr.

2. DATA

2.1. Observations & Data Reductions

Spectra of the emission candidate members of Abell 851 were obtained using the Keck I LRIS and Keck II DEIMOS on the nights of 2002 January 6-8 and 2003 January 26-27, respectively. These observing runs were made in photometric conditions, with seeing of $0''.7-0''.8$, measured with two-dimensional spectra of standard stars; the seeing appeared slightly worse during DEIMOS observations.

All the LRIS spectra analyzed in this paper were obtained using the D460 dichroic with the 600/4000 grating. The spectral coverage was $\sim 5000-7000 \text{ \AA}$, enough for the inclusion of the redshifted [O II] λ 3727 up to [O III] λ 5007, but not H α for the objects at the redshift of interest. There were six different multislit masks, each with 20–25 slits. The slit width was fixed at $1''$, yielding the spectral resolution of $\simeq 4.8 \text{ \AA}$ FWHM of arc lines. For most masks, the total exposure time was 7200 seconds. Our LRIS data were reduced using the standard IRAF⁵ facilities along with custom PyRAF⁶ scripts for the most common tasks. The individual frames were bias subtracted and corrected for pixel-to-pixel sensitivity variations. The science frames for each mask were then coadded with the cosmic-ray rejection option after being registered using the positional cross-correlation of bright emission features.

All DEIMOS spectra were obtained using the 600 lines/mm grating and the GG495 filter. A total of five multislit masks, each with 40–50 $1''$ -slits, were used. The spectral resolutions were $\simeq 2.7 \text{ \AA}$ and $\simeq 3.2 \text{ \AA}$ FWHM of arc lines for blue and red sides, respectively. The total exposure times were 9000, 9000, 10800, 5195, and 10800 seconds for these masks. The DEEP2 DEIMOS data pipeline⁷ was used to produce final one-dimensional spectra of DEIMOS observations. Before flux calibration, these one-dimensional spectra were converted with a purpose-written Python program into FITS images that can be processed on IRAF or PyRAF, with which most subsequent data analysis were made. All one-dimensional spectra were linearized and rebinned to 1.28 \AA and 0.65 \AA per pixel for the LRIS and DEIMOS spectra, respectively.

We also make use of Sloan g and i photometry from the MLF00 imaging survey.⁸ For the detail on the broadband photometry, see MLF00.

All target spectra were flux-calibrated with Kitt Peak spectrophotometric standards (Massey et al. 1988). In the LRIS observations, the standards were observed with a longslit mask ($1.5'' \times 175''$). For the DEIMOS run, a slitless spectrum was obtained for each standard star. We did not correct for foreground Galactic reddening toward the target field, as it is

⁵ IRAF (Image Reduction and Analysis Facility) is distributed by the National Optical Astronomy Observatories, which are operated by AURA, Inc., under cooperative agreement with the National Science Foundation.

⁶ PyRAF is a product of the Space Telescope Science Institute, which is operated by AURA for NASA.

⁷ The analysis pipeline used to reduce the DEIMOS data was developed at UC Berkeley with support from NSF grant AST-0071048.

⁸ There was a +0.43 mag error in the MLF00 g photometry as a result of an error in the previously published Abell 851 g photometry (Dressler & Gunn 1992) used for their original calibration (Lotz et al. 2003). In this paper, we have recalibrated our g photometry as in Lotz et al. (2003), such that $g-i = (g-i)_{\text{MLF00}} - 0.43$.

TABLE 1
SPECTROSCOPIC TARGET SELECTION

Color	Spectroscopic Targets	[O II] Emission Candidates	Correction Factor
$g-i < 1$	71	100	1.41
$1 < g-i < 2$	89	135	1.52
$2 < g-i$	31	81	2.61
N/A ^a	18	55	3.06

NOTE. — Correction factors are the number of [O II] emission candidates divided by the number of spectroscopic targets.

^a Objects with their uncertainty in $g-i$ color exceeding 0.5.

marginal at $E(B-V) \simeq 0.016$ (Schlegel et al. 1998) compared to the average intrinsic reddening of target galaxies.

In reality, absolute flux calibration does not necessarily yield a physically reliable estimate of source flux from the region of interest due to various observational systematics. The spatial coverage of a target depends on the aperture size relative to the source, causing aperture effects. A slight offset in the alignment of slit mask during different exposures introduces systematics as well. The alignment effect appeared relatively small, as the repeat observations with the same instrument yielded the variation within a factor of $\simeq 2$ in the mean continuum flux densities within the rest-frame 4150–4300 Å (§ 2.2). Among the repeat observations with the different instruments, the mean continuum flux was smaller by a factor of $\simeq 2$ for a vast majority, but not all, of DEIMOS spectra. Since both the LRIS and DEIMOS observations were made with the same aperture size in photometric conditions, we suspect the slit alignment may have been worse in the DEIMOS observations; slightly worse seeing during the DEIMOS run may have also contributed to the discrepancy.

In MLF00 the [O II] emission candidates were selected based on the S/N of on-band flux excess through the on-band narrowband filter, with the continuum narrowband filter blueward of on-band. The choice of this specific narrowband filter was made based on the redshift ($z = 0.4067$) and cluster velocity dispersion ($\sigma_v = 860 \text{ km s}^{-1}$) reported by Dressler & Gunn (1992) to ensure that the redshifted [O II] $\lambda 3727$ emission line from a majority of the virialized cluster members fall within its passband. A total of 371 objects with the on-band flux excess at $S/N > 3$ level made the category of *on-band-selected sample* of emission-line galaxy candidates. Due to the limited wavelength coverage of LRIS data, our DEIMOS run had a significant number of repeat observations of LRIS objects to ensure simultaneous detection of [O II] and H α emissions. A total of 212 on-band-selected targets were observed in this spectroscopic follow-up; in three of these targets we could not detect significant continuum, reducing the sample size to 209.

The spectroscopic targets, drawn from the MLF00 on-band-selected sample, were mostly selected by their $g-i$ color, favoring bluer objects; no further S/N cut was made within this spectroscopic sample. MLF00 divided the [O II] emission candidates into three $g-i$ color categories: blue ($g-i < 1$), green ($1 < g-i < 2$), and red ($g-i > 2$). The objects with poor photometry (i.e., the uncertainty in $g-i$ color exceeding 0.5) are excluded from these categories, constituting “gray” (in MLF00) or N/A objects. Our initial intention was to make the $g-i < 1$ sample as complete as possible, since true [O II] emitters are expected to have a blue $g-i$ color in general. However, a calibration error in the original photometry shifted many objects into the $g-i < 1$ category for this spectroscopic follow-up, making our $g-i < 1$ sample

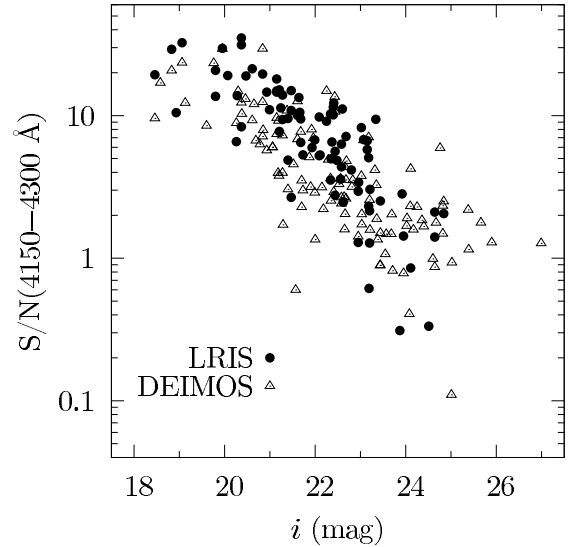


FIG. 1.— Continuum S/N per pixel of spectra as a function of their source i magnitude. See § 2.2 for the definition of continuum S/N.

TABLE 2
SPECTRAL LINE INDEX DEFINITIONS

Line	Blue continuum (Å)	Line (Å)	Red continuum (Å)
[O II] $\lambda 3727$	3653–3713	3713–3741	3741–3801
H δ	4030–4082	4082–4122	4122–4170
H γ	4230–4270	4320–4359	4367–4383
H β	4785–4815	4821–4901	4925–4949
[O III] $\lambda 5007$	4960–4985	4993–5021	5030–5055
H α	6493–6532	6553–6574	6596–6636
[N II] $\lambda 6583$	6493–6532	6574–6593	6596–6636

larger in number but less complete (Table 1).

If repeat observations existed, the spectrum with the highest continuum S/N (§ 2.2) was generally used for analysis (i.e., the *highest-S/N spectrum*) unless a significant defect was noted for that spectrum upon visual inspection, in which case the spectrum of the second highest S/N was used. At times we supplement our data by using a lower-S/N spectrum if the spectral range of the highest-S/N spectrum does not cover spectral features of interest; we indicate the use of such *secondary spectrum* where appropriate.

2.2. Spectral Line Measurements

To compute characteristic signal-to-noise ratio (S/N) of a spectrum, a 3rd-order polynomial was fitted to the continuum within the rest-frame wavelength range of 4150–4300 Å with two iterations of sigma clipping at $\pm 2\sigma$, where σ is the RMS residual noise per pixel. The mean flux density of the fit within the spectral range was divided by σ to obtain the continuum S/N per pixel. The resulting continuum S/N distribution is shown in Fig. 1. A large number of spectra of varying qualities prompted us to standardize the measurement process with purpose-written software employing two methods of line measurement, suitable for different purposes.

2.2.1. Gaussian-Fitting Method

For each spectral line, a straight line was fitted to the continuum flux blueward and redward of a line to estimate the continuum flux density. The linear baseline was then subtracted from the spectral line region, over which either one or

two Gaussian profiles were fitted to the spectrum, depending on the presence of emission, absorption or both lines. These spectral ranges are predefined (Table 2). The results of the fit were inspected visually for all the spectral features, and the spectral ranges were often adjusted to avoid data points obviously affected by anomalies such as telluric features and cosmic rays.

Some Balmer lines, e.g., $H\beta$, $H\gamma$, and $H\delta$, often show both emission and absorption lines. In such cases, emission and absorption line fluxes were computed separately from the best fit parameters of each Gaussian. The uncertainty in the line flux thus obtained was estimated from the RMS of the Gaussian profile over the spectral line region, multiplied by $\sqrt{N\Delta\lambda}$, where N is the number of data points used in the fit, and $\Delta\lambda$ is the dispersion of the spectrum per pixel.

There is an intrinsic difficulty in separating the nebular and stellar components in Balmer lines. As described above, these components were fitted with two Gaussians when they were visually identified. For low-S/N spectra, this was often not possible, and only an emission or absorption feature was fitted. The Balmer absorptions in the stellar atmosphere are presumably always present, however, and we underestimate an emission flux in presence of undetected absorption flux (or vice versa). When appropriate, we corrected emission flux artificially by adding an equivalent width of 2 Å at $H\alpha$, $H\beta$, and $H\gamma$ (McCall et al. 1985), if absorption features were not explicitly fitted.

2.2.2. Flux-Summing Method

The continuum baseline near a line was estimated as in the Gaussian-fitting method (§ 2.2.1). The line strength was measured by summing the differences between the observed spectrum and the continuum baseline over the spectral line region. The uncertainty in this strength was estimated by summing in quadrature the values stored in the sigma vector of 1D spectrum and the RMS of continuum fit for all pixels in the spectral line region. The measurements through this method were done uninteractively using the redshifts computed from the line centers measured from the Gaussian-fitting method (§ 2.3). The uncertainty in the continuum flux at the line center was determined from the RMS of linear fit divided by the square root of number of data points used in the continuum fitting.

For both the above methods, the line or continuum fitting was done by a standard nonlinear least-square regression routine with variance weighting using the formal sigma vector computed for each 1D spectrum in the data reduction process. For each line feature, its equivalent width W was computed from

$$W = -\frac{F}{F_\lambda},$$

where F is the line flux and F_λ is the continuum flux density at the line center. We use the sign convention where $F > 0$ for lines in emission and $F < 0$ for lines in absorption; therefore the equivalent width is negative for a pure emission line and is positive for a pure absorption line. We use this sign convention throughout the paper. At times sticking to this convention can cause confusion, since we often use a word increase (decrease) to mean the *magnitude* of equivalent width increases (decrease), deviating from its mathematical sense. For example, an equivalent width growing in emission means the value is getting more negative. Therefore we caution that contextual interpretation is sometime necessary when the behavior

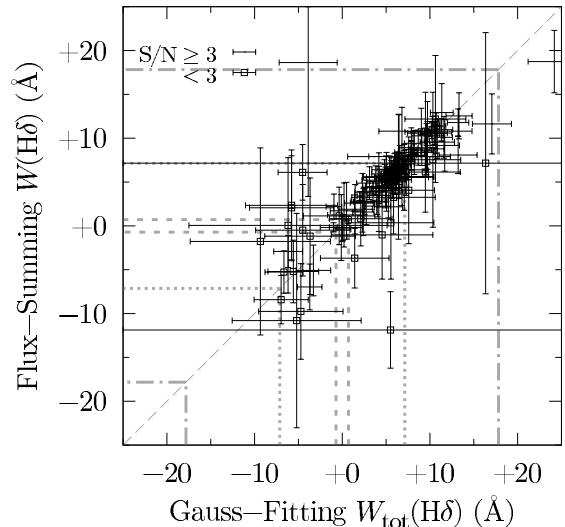


FIG. 2.— $H\delta$ equivalent widths from two different measurement methods (§ 2.2). $W_{\text{tot}}(H\delta)$ is computed from the sum of emission and absorption equivalent widths using the Gaussian-fitting method. Open squares denote measurements for which $S/N < 3$, where S/N here is the flux density at line center divided by the RMS noise derived from the straddling continua, i.e., a measure of spectral quality insensitive to the strength of $H\delta$ line flux. The dashed gray line indicates loci of equality. The dashed, dotted, and dash-dotted lines indicate the minimum (absolute) equivalent widths that can be measured with S/N of 10, 1, and 0.4, respectively, at the LRIS dispersion, 1.28 Å per pixel.

of equivalent widths is discussed, i.e., we may often not use expressions that strictly follow mathematical senses. We distinguish the observed and rest-frame quantities by the use of subscript with zero, e.g., W and W_0 are observed and rest-frame equivalent widths, respectively.

Note that the equivalent width from the flux-summing method estimates the total flux in a line, i.e., the sum of emission and absorption fluxes, relative to the continuum flux density at the line center. This method has a disadvantage that the distinction between nebular emission and stellar absorption, for example, cannot be made from its measurements even when these features are well resolved. Although the spectral dispersion was good enough to resolve emission and absorption lines in many cases, there were difficulties identifying spectral features for low-S/N spectra. The Gaussian-fitting method, requiring visual attention, is not effective for those spectra for obvious reasons. In addition, the effect of emission filling in absorption features may not be apparent in low-quality spectra.

The flux-summing method does not directly yield physically meaningful measurements when line features are complex, but has an advantage in that faint features can be measured statistically. Hence the flux-summing method is suitable for indexing spectral features, being less dependent on the quality of spectra. The Gaussian-fitting method is the preferred method for extracting physically meaningful information such as line ratios used in emission-line diagnostics. The two methods generally yield consistent results except for very low-S/N measurements (Fig. 2).

Hence we used the flux measurements from the Gaussian-fitting method if both emission and absorption are present at a line and need to be separated to each component, which is the case when emission-line flux ratios involving Balmer lines are desired, for example. Since our analysis mostly is on emission line properties, the Gaussian-fitting method extracts the emission component when absorption is also present. With low-

S/N spectra or very emission-dominated line (such as $H\alpha$) for which visually fitting the two components are not possible, we assumed a fiducial amount of underlying absorption flux to be present, and corrected emission flux accordingly (§ 2.2.1). We used the flux-summing method mostly to *index* spectral properties, e.g., placing galaxies in [O II]- $H\delta$ equivalent width plane to identify post-starburst galaxies in our forth-coming paper. In other words, we did not use flux-summed measurements to push measurements toward very faint emission line flux in general.⁹

2.3. Redshift Determination

The redshift was estimated from the central wavelength of all the line profiles using the Gaussian-fitting method. Since emission and absorption lines were fitted separately when both were visually identified, the redshifts were computed separately for them as well. The best estimate and its standard deviation are simply computed from the list of redshifts thus obtained for each spectrum. Although no weights were assigned for the line features, any redshift measurement beyond 1σ were rejected before the final determination of redshift for that spectrum.

2.3.1. Cluster Membership

In MLF00 narrowband survey, cluster membership was simply assumed for the objects for which a candidate [O II] $\lambda 3727$ emission line was detected within the on-band filter. Note that more up-to-date estimates of cluster velocity dispersion give higher σ_v for Abell 851 than the one used to design the original survey; at $\sigma_v = 1260 \text{ km s}^{-1}$ (Dressler et al. 1999), about 75% of virialized cluster members would have been detected, which is a lower fraction than originally intended. We classified an object to be a cluster member if its redshift was within $0.395 < z < 0.420$, corresponding to the on-band filter used in MLF00 [O II] narrowband search (approximately $5198.7 - 5290.6 \text{ \AA}$).

3. CONFIRMATION OF [O II] EMITTERS

MLF00 discussed the likelihood of falsely detecting an emission line or steep continuum profile of foreground or background object in their narrowband search. Their conclusions were as follows: (1) While the 4000 \AA break of the foreground early-type galaxies would be a major cause of false detection in the [O II] narrowband search, they could be distinguished by their red $g-i$ colors; (2) the small survey volume meant prominent [O III] $\lambda\lambda 4959, 5007$ doublet and the $H\beta$ emission of low- z interlopers would produce only a small number of false detection; and (3) considering the competing effects of increasing survey volume and decreasing apparent brightness at high z , background $\text{Ly}\alpha$ emitters were not likely to produce a significant number of false detections.

3.1. True Detection Rate

To evaluate the efficacy of [O II] narrowband search, we used a subset of spectra for which the on-band filter passband ($5198.7 - 5290.6 \text{ \AA}$ or $0.395 < z < 0.420$ for [O II] $\lambda 3727$) was fully within the observed spectral range for that spectrum, i.e., the aperture location on a slit mask and/or dispersion did not move the MLF00 on-band out of usable portion of CCD chip. Based on this criterion, we rejected 29 targets from the 209

spectroscopic targets, reducing the total number of galaxies to 180.

We used a simple criterion for a true detection of [O II] emission. For an object to be classified as a confirmed [O II] emitter, it had to have $W([\text{O II}]) < -11 \text{ \AA}$ measured both in the Gaussian-fitting and in the flux-summing methods (§ 2.2); the equivalent width cut roughly corresponds to the narrowband survey detection limit of MLF00. The spectrum that did not satisfy this criterion either was of a very low-S/N or would indicate a true non-detection in our definition; the distinction was made such that the true non-detection of [O II] for an object meant that its spectroscopic S/N was high enough that $W([\text{O II}]) < -11 \text{ \AA}$ could have been detected at 2σ level. To better reproduce the observing condition of MLF00 survey, the continuum S/N was computed using the RMS noise within the wavelengths corresponding to the MLF00 on-band filter passband after three iterations of $\pm 2\sigma$ clipping.

In Table 3, we show how the true detection rates break down by $g-i$ color. The subset of sample used for the analysis is first divided into those with redshift measurements and without. The subset with no redshifts consists of two types of objects. Since our primary interests were [O II] emitters, we did not measure the line features of apparently early-type spectra, leaving redshifts unknown for most absorption-dominated objects. The rest of the objects with no redshifts have low-S/N spectra such that no line features could be measured, leaving their redshifts unknown. For the subset with redshifts, secure detection of lines, not necessarily including [O II] $\lambda 3727$, were made that redshifts could be measured. Not surprisingly, all the spectra in this subset had good enough S/N for detecting the [O II] equivalent width at the predefined significance level; we used the criterion as mentioned above for distinguishing low-S/N spectroscopic object from true non-detection. The cluster membership was simply assumed for an object whose redshift moved the central wavelength of its [O II] $\lambda 3727$ emission line into the on-band filter passband.

Table 3 shows that the true detection rate strongly depends on the $g-i$ color of objects, generally confirming the conclusions drawn by MLF00. Most $g-i < 1$ objects turned out to be true [O II] emitters with very high successful detection rate ($\simeq 85\%$). One of the five false detections of $g-i < 1$ objects was Mg II $\lambda 2798$ emission line of a $z \simeq 0.87$ object; others were detection of 4000 \AA break from objects at $z \simeq 0.47$ (1) and at $z \simeq 0.31$ (3).

For $1 < g-i < 2$ objects, the true detection rate was lower, in part due to the stricter definition of true [O II] detection employed in this analysis, requiring $W([\text{O II}]) < -11 \text{ \AA}$. Five of the seven cluster members classified into no [O II] emission category have visually detectable [O II] emission, and the remaining two exhibited a typical post-starburst spectrum with little or no [O II] emission; in fact, strong Balmer absorption lines and a prominent 4000 \AA break appeared common among this category. The false detections of non-member $1 < g-i < 2$ objects were caused by 4000 \AA break from the objects at $z \simeq 0.35$ (3) or $z \simeq 0.39$ (2) and by unknown reasons for the objects at $z \simeq 0.62$ and 0.53 .

Most of $g-i > 2$ objects were false detections of early-type galaxy spectra or possibly a few late-type K- or M-type stars which showed few or no emission lines, and therefore their redshifts were not measured. In three $g-i > 2$ objects we detected [O II] emission line: one luminous object with a typical early-type galaxy spectrum but also with emission lines—

⁹ An important exception is made for a pure emission line such as [O II] $\lambda 3727$, for which no absorption correction is necessary.

TABLE 3
[O II] TRUE DETECTION RATE BY $g-i$ COLOR

Color	N^a	No Redshift			With Redshift			Rate (%)
		Low S/N ^b	Other ^c	Low S/N ^b	Non-Member ^d	No [O II] ^e	True [O II] ^f	
$g-i < 1$	63	9	3	0	5	0	46	85.2
$1 < g-i < 2$	80	5	11	0	7	7	50	66.7
$2 < g-i$	24	5	16	0	0	0	3	15.8
N/A ^g	13	6	2	0	0	0	5	71.4

NOTE. — True detection of [O II] emission required $W([O II]) < -11 \text{ \AA}$ at 2σ level. Low-S/N targets were excluded in the computation of true detection rate (last column).

^aTotal number of MLF00 [O II] emission candidates included in the true detection rate analysis.

^bOn-band spectroscopic S/N too low to detect [O II].

^cHigh enough on-band S/N for [O II] detection but the line visually undetected.

^dMeasured redshift moved [O II] outside the on-band filter passband.

^e[O II] expected within the on-band from the measured redshift but not detected.

^f $W([O II]) < -11 \text{ \AA}$ detected within the on-band.

^gObjects with their uncertainty in $g-i$ color exceeding 0.5.

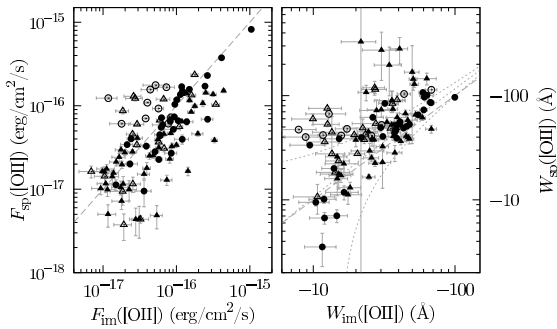


FIG. 3.— Comparison of [O II] λ 3727 emission line flux (*left*) and equivalent width (*right*) measured in MLF00 narrowband imaging and this spectroscopic follow-up. Circles and triangles denote LRIS and DEIMOS spectra, respectively. Filled and open data points denote on-band and on-edge samples, respectively (§ 3.2). The gray dashed lines indicate the loci of equality. For the right figure, the dotted curves indicate a linear fit and $\pm 1\sigma$ bounds to the on-band sample. The final σ was computed after one iteration of $\pm 1\sigma$ clipping. Upon fitting each data point was given a weight of $1/\sigma^2$, where σ is the sum in quadrature of the two measurement errors in imaging and spectroscopic equivalent widths.

an elliptical galaxy hosting a low-luminosity AGN; one very faint object with a spectrum in which only [O II], [O III], and Balmer lines could be visually identified; and one object with a spectrum which appeared a superposition of two different objects.

The results have shown that a narrowband technique is a very effective method of selecting emission-line galaxies, but the true detection of emission-line galaxies requires some constraints to be put on their photometric properties.

3.2. [O II] Line Flux Measurements

With the systematic errors in flux calibration (§ 2.1), analysis using absolute fluxes may be unreliable. In Fig. 3, [O II] λ 3727 flux and equivalent width measured from spectra and MLF00 narrowband imaging are compared. The comparisons of the two sets of independent measurements are complicated by several factors. First, an on-band flux excess from narrowband imaging was only a lower limit of a total integrated emission flux if at least a portion of the redshifted [O II] line profile fell on the steeply declining portion of the on-band filter transmission curve. Second, a spectroscopic flux of our multislit spectroscopic sample were only a lower limit to the total [O II] emission flux from a galaxy due to an aperture effect. In this case, both the relative size of the aperture and the galaxy and misalignment of an aperture with respect to

the galaxy center could produce noticeable systematics, because the composition of the stellar populations covered by the aperture (e.g., bulge and disk) may change significantly. Since each $1''$ -width slit was supposed to be aligned to the center of each galaxy with a typical angular size of $\sim 3''$ – $4''$ in diameter, each spectrum was spatially sampling only around a nuclear region extending over roughly ~ 10 kpc. Third, in MLF00 only the continuum band placed blueward of [O II] emission was used to estimate the continuum flux density near [O II] emission. This may cause discrepancy in the [O II] flux and equivalent width measurements, as the [O II] emission appears near the 4000 \AA break.

To see the effect of incomplete integration over a line profile in narrowband photometry, we divided the sample into three categories. Using the central wavelength λ_c of redshifted [O II] emission line profile, there are (1) an *on-band sample* consisting of those objects with $5222.5 \text{ \AA} \leq \lambda_c < 5264.9 \text{ \AA}$ for which the transmission efficiency is over 0.7; (2) an *on-edge sample* either with $5197.0 \text{ \AA} \leq \lambda_c < 5222.5 \text{ \AA}$ or with $5264.9 \text{ \AA} \leq \lambda_c < 5292.0 \text{ \AA}$; and (3) an *off-band sample* either with $\lambda_c < 5197.0 \text{ \AA}$ or with $\lambda_c \geq 5292.0 \text{ \AA}$, where the transmission efficiency drops below 10^{-3} . Since the off-band sample are not cluster members under the definition used in this paper, they are excluded from this analysis.

In Fig. 3 the major outliers above the line of equality tend to be of on-edge sample, and the narrowband [O II] measurements generally are smaller than those of spectra. This discrepancy can be easily attributed to the incomplete integration over a [O II] line profile, i.e., the narrowband flux gets underestimated while the off-band continuum remains relatively unchanged, giving smaller equivalent width. Within the on-band sample for which the narrowband flux is a good estimate for the total [O II] emission flux, the spectroscopic flux generally underestimates the [O II] flux due to aperture effect.

To see if the relative size of the aperture and galaxy, misalignment, or the discrepancy in the determination of narrowband continuum flux density near [O II] contributes significantly to systematics, we plotted the ratio of spectroscopic to MLF00 narrowband imaging measurements against the source isophotal area from the MLF00 narrowband survey and the ratio of spectroscopic to imaging [O II] continuum flux densities in Fig. 4.

If the relative size between the aperture and galaxy was a major cause of discrepancy between narrowband and spec-

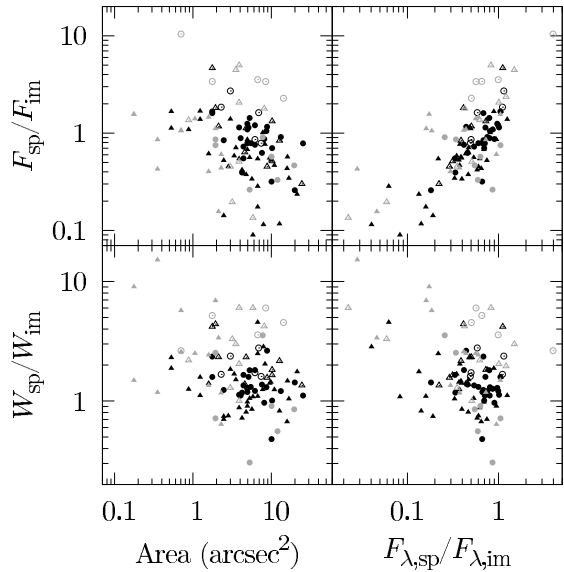


FIG. 4.— Distribution of discrepancies in imaging and spectroscopic measurement of [O II] flux (*top row*) and equivalent width (*bottom row*) by the source isophotal angular size (*left column*) and the discrepancy in the [O II] continuum flux densities (*right column*) determined by MLF00 narrowband imaging and this spectroscopic studies. The measurements for which the $S/N < 5$ for on-band imaging flux excess and spectroscopic flux density at the line center are grayed out. The definition of symbols are identical as in Fig. 3.

troscopic measurements, we would expect the agreement between the two measurements to be better for smaller galaxies. The upper left plot of Fig. 4 suggests the flux loss for larger galaxies is indeed significant. The upper right plot shows a strong positive correlation between the discrepancy in [O II] flux and the continuum flux density measurements. Notably our flux-calibrated spectra could underestimate *both* [O II] emission flux and continuum flux density by up to a factor of ~ 3 , ignoring possible outliers for which the ratios were $\lesssim 0.3$. The linear correlation, which appears to be followed, is expected if the discrepancy between narrowband and spectroscopic measurements is dominated by the systematic error in flux calibration. The upper plots appear to suggest the presence of aperture effect and systematic error in flux calibration.

The corresponding trends are harder to observe in lower plots, comparing spectroscopic and narrowband equivalent widths. Spectroscopic [O II] equivalent widths are slightly greater in general than those from narrowband measurements. The sloping continuum of the Balmer break around [O II] $\lambda 3727$ usually causes the continuum blueward of the line to have lower flux density than that of the redward continuum. We suspected this underestimate of continuum flux density at [O II] might cause narrowband [O II] emission equivalent widths to become systematically stronger, but the effect appears negligible.

If we suppose the underestimate of spectroscopic flux is caused by the aperture effect and/or misalignment, it is only to the extent that the underlying stellar population covered by the aperture does not change substantially because the equivalent width measurements show little trend with the source isophotal area and the discrepancy of their continuum flux densities. However, the plots do indicate a few low-S/N measurements yield very large equivalent widths, probably due to poorly defined continuum flux density.

We conclude that our flux-calibrated spectra can yield underestimates by a factor of up to ~ 3 for absolute physical quantities due to the combination of aperture effect, misalign-

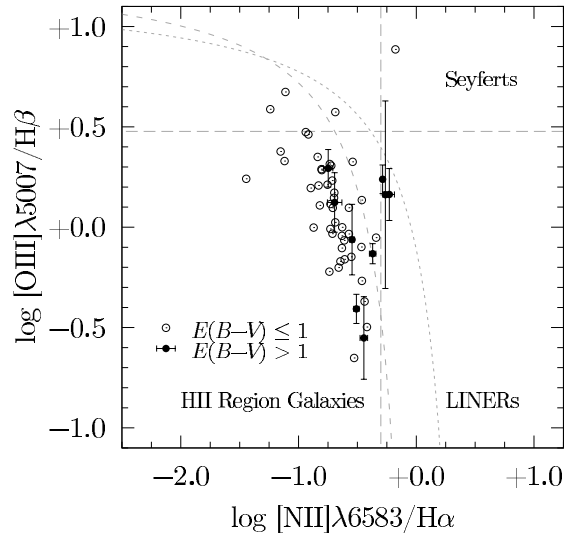


FIG. 5.— Line ratio diagnostic diagram for [N II] $\lambda 6584$ vs. [O III] $\lambda 5007$ normalized to the nearest Balmer emission line. The classifications indicated follow the scheme of Ho (1996), but the cut was made at [N II]/ $H\alpha = 0.5$ instead of 0.6. The demarcation defined by Kauffmann et al. (2003) (dashed curve) and Kewley et al. (2001) (dotted curve) are also shown for comparison. Galaxies with high dust reddening [$E(B-V) > 1$] are separately indicated with their error bars.

ment, and systematic error in flux-calibration but only to the extent that the equivalent widths remain robust. We also note there also was a slight seeing variation which would affect flux measurements. At least some of unusually large spectroscopic [O II] equivalent widths are likely to be caused by large uncertainties in the continuum flux density near [O II] emission line.

4. PROPERTIES OF THE CLUSTER [O II] EMITTERS

4.1. AGN Diagnostics

Some of the observed [O II] emission could be from active galactic nuclei (AGNs). In Fig. 5 we show a line ratio diagnostics diagram for AGN activity using the scheme outlined in Ho (1996). Only the objects with measured line fluxes necessary to compute the diagnostic ratios are in the diagram. A similar diagram using [S II] $\lambda\lambda 6716, 31$ doublet was not made since the lines were outside the observed window or severely compromised by sky lines. We deviated from their scheme in that the distinction between AGN-like and H II region-like galaxies was made at [N II] $\lambda 6583/H\alpha = 0.5$, instead of 0.6, to include objects whose spectra apparently have broad emission lines upon visual inspection. This criterion identifies a total of 7 galaxies to be AGN-like, 3 of which cannot be plotted in Fig. 5 for their lack of either [O III] or $H\beta$ measurements. For comparison, more recent demarcation from Kauffmann et al. (2003) and Kewley et al. (2001) are also shown. We see that the AGN identification is indeed sensitive to the choice of demarcation, yet we keep the above criterion since it does remove objects with visually identifiable broad emission lines. The diagnostic line fluxes are not corrected for reddening, but taking a ratio to the nearest Balmer line, e.g., [O III] $\lambda 5007/H\beta$ and [N II] $\lambda 6583/H\alpha$ minimizes the effect of reddening; applying reddening correction did not change the results significantly. In order to include more objects in this diagnosis, however, we deviated from our convention of using the best S/N spectrum and used a secondary spectrum if AGN diagnostics cannot be done otherwise (§ 2.1); if a spectrum from a repeat observation at a lower S/N but with both [N II] $\lambda 6583$ and $H\alpha$ measurements

exist, we used that spectrum to do the AGN diagnostic.

As far as their $g-i$ colors are concerned, it is hard to distinguish AGN-like galaxies from the rest of the [O II] emitters, although they are found mostly toward the bright end in the color-magnitude diagram. It should also be noted that our AGN-like galaxies are not detected in previous X-ray observations; we will discuss the implication of these results in a forth-coming paper in the series. Most cluster [O II] emitters are classified as normal star-forming, H II region-like galaxies. Where appropriate, 7 objects identified to be AGN-like will be removed from subsequent analysis of star-forming galaxies.

4.2. Derivation of $E(B-V)$

We derived reddening $E(B-V)$ from the Balmer decrement of either $H\alpha/H\beta$ or $H\gamma/H\beta$ emission line flux ratio, depending on the availability of the lines, with the presumed theoretical line ratios of $(H\alpha/H\beta)_0 = 2.85$ and $(H\gamma/H\beta)_0 = 0.469$ for Case B recombination at $T_e = 10^4$ K and $n_e = 10^4$ cm $^{-3}$ from Osterbrock (1989). The relation to convert the observed flux F into the intrinsic flux F_0 is

$$F_0 = F 10^{0.4E(B-V)k^e(\lambda)},$$

where $k^e(\lambda)$ is the extinction curve described in Calzetti et al. (2000). Being derived from a ratio of nebular emission lines, $E(B-V)$ therefore is the amount of reddening in the nebular component, which is generally greater by a factor of ~ 2 than that measured in the stellar component (e.g., Calzetti et al. 1994).

Unfortunately, the spectral region around the redshifted H β often suffer from a telluric absorption feature near ~ 6870 Å, so the quantities derived partially from H β measurements tend to have large uncertainties. We emphasize that the high uncertainty in our H β measurements is largely the consequence of deriving the uncertainty in line flux from the RMS of Gaussian fit, but it is the H β *absorption profile* which gets partially contaminated by the telluric feature at the redshift of interest. The Gaussian fitting itself was done with weighting by inverse variance, which includes the uncertainty due to sky subtraction (§ 2.2). Therefore we may have overestimated the uncertainty in emission flux, which is almost never compromised by the same sky line. We also make clear that at H β the emission and absorption profiles could almost always be fit separately; therefore the derived $E(B-V)$ do not get overestimated from possible underestimation of underlying absorption at H β (§ 2.2.1).

4.3. [O II]/H α Ratio & Star Formation Rate

The empirical correlation between [O II] λ 3727 emission line and H α fluxes calibrated by Gallagher, Hunter, & Bushouse (1989) and Kennicutt (1992) is often used to estimate star formation rate (SFR) of distant galaxies, since the [O II] doublet is the strongest emission line in the blue that remains available within the optical range for high- z galaxies. In Fig. 6 we show the dependence of the observed [O II]/H α line flux ratio on the amount of reddening $E(B-V)$ and galaxy luminosity. The absolute V -band magnitudes, M_V (on the Vega scale), are derived from the reddening-corrected g and i photometry using software package `kcorrect` (v4_1_4; Blanton et al. 2003).¹⁰ The relative independence of [O II]/H α on dust

¹⁰ The objects for which we could not derive reddening $E(B-V)$ from their line ratio are therefore removed from the current analysis.

reddening after correction is one of the basic assumptions for the reliability of [O II] λ 3727 emission as a star formation indicator. To compare with previous studies, we compute the mean [O II]/H α for the [O II] emitters identified to be regular H II region-like galaxies (§ 4.1). Before reddening correction, the mean ratio of [O II]/H α = 0.56 ± 0.01 is comparable to 0.57 ± 0.06 and 0.73 ± 0.03 measured by Kennicutt (1992) and Jansen et al. (2001), respectively. After correction, the ratio becomes 0.88 ± 0.08 for our sample, which is slightly lower than 1.1 ± 0.1 and 1.2 ± 0.3 obtained by the aforementioned studies. The ranges of luminosities in these samples are roughly consistent with each other.

The range of $E(B-V)$ in Fig. 6 implies a significant fraction of [O II] emitters suffers high degree of dust reddening. Whereas the galaxies Kewley et al. (2004) used for their calibration of SFR mostly have the extinction of $E(B-V) \lesssim 0.5$, a significant fraction of our cluster [O II] emitting sample has $E(B-V) > 0.5$. It is well known that optical diagnostic methods such as [O II] λ 3727 emission line flux severely underestimate the amount of star-formation activities in presence of high dust reddening, when no extinction correction is made. Although a very strong trend with $E(B-V)$ is removed by reddening correction, the ratio [O II]/H α for very dusty galaxies remains about a factor of two lower than the mean for the entire sample. Indeed the low [O II]/H α ratio of the high- $E(B-V)$ galaxies caused our mean [O II]/H α to be lower than the ratios measured by previous studies mentioned above. Based on the figure, the reliability of the widely used SFR calibration between [O II] and H α emission lines (e.g., Kennicutt 1998) may not extend to very dusty galaxies in general, e.g., $E(B-V) \gtrsim 0.7$, which appear abundant in high- z universe and have been reported to show smaller [O II]/H α as well (Hicks et al. 2002). Furthermore, the uncorrected [O II]/H α shows a modest trend with luminosity in Fig. 6. Although reddening correction appears to remove the luminosity trend, a few very low-[O II]/H α galaxies do not move closer to the mean ratio. In fact, these are $E(B-V) > 0.5$ galaxies, and their distribution in luminosity does not appear to show a strong trend.

As reported by Jansen et al. (2001), the relations among the [O II]/H α ratio, dust reddening, and luminosity appear coupled, yet our cluster [O II] emitting sample in Fig. 6 shows that [O II]/H α has the strongest trend with the amount of dust reddening, and for very dusty galaxies, their [O II]/H α ratio remains lower than the locally measured means regardless of their luminosity. The primary reason for this trend may be the dependence of [O II]/H α ratio on the ionization state and the gas phase metallicity of emission nebula as reported in metal-rich (Kewley et al. 2004) and metal-poor galaxies (Mouhcine et al. 2005). To study the relevance of [O II]/H α ratio further, it is necessary to constrain and consider the gas-phase metallicity and ionization state of galaxies in our sample.

4.4. [O II] Emission & Luminosity

The mass associated with the stellar component of a galaxy is better traced in redder passbands, which measure flux from the part of galaxy spectrum relatively insensitive to the recent star formation history and also suffers less dust extinction. The reddest imaging in our survey is Sloan i , so we could take the observed i magnitude as the quantitative estimate for the underlying stellar mass, or more generally the size, of a galaxy. In the cluster rest-frame the Sloan i filter really samples the V -band light of galaxy spectrum. Thus i magnitude

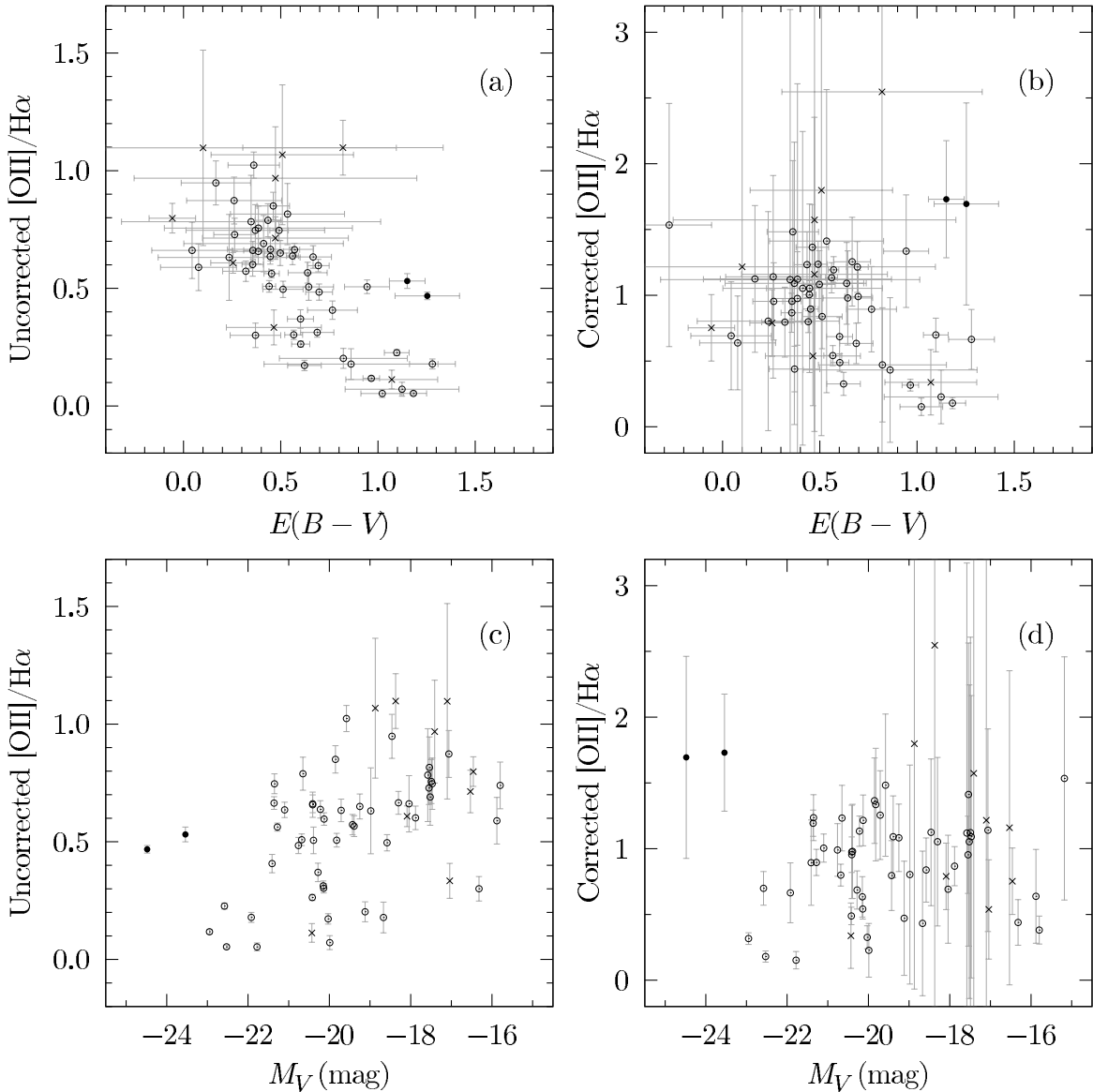


FIG. 6.— The distribution of emission line flux ratio $[\text{O II}]/\text{H}\alpha$ as a function of reddening $E(B-V)$ derived from a Balmer decrement, (a) before and (b) after extinction correction. The ratio $[\text{O II}]/\text{H}\alpha$ as a function of absolute V magnitude (c) before and (d) after extinction correction are also plotted. Open and filled circles are $[\text{O II}]/\text{H}\alpha$ of normal, H II region-like galaxies and AGN-like objects, respectively (§ 4.1). Crosses are the objects whose classification by the line ratio diagnostics could not be carried out.

is not the best proxy for the underlying stellar population that dominates the stellar mass composition of a galaxy. An instantaneous burst model of Bruzual & Charlot (2003) shows that at 10 Myr a starburst fraction of only $\sim 1\%$ can make a dominant contribution to the visual spectrum at $\sim 5500 \text{ \AA}$ on top of 10 Gyr-old stellar population. Although we use extinction-corrected absolute V magnitude to estimate the intrinsic luminosity or size of galaxies, some caution should be exercised to interpret our results, as the quantities are highly dependent on their SFHs.

Previous studies have noted that the $[\text{O II}]$ equivalent widths tend to anti-correlate with luminosity (Cowie et al. 1996; Hogg et al. 1998; Blanton & Lin 2000; Charlot et al. 2002). In Fig. 7, we observe similar trend in $[\text{O II}]$ and $\text{H}\alpha$ equivalent widths (measured with the flux-summing method). Since the completeness limit of MLF00 survey was $W([\text{O II}]) \simeq 11 \text{ \AA}$ at $i \simeq 23$ ($M_V \simeq -19$), the lack of intrinsically faint weak $[\text{O II}]$ emitters is partly a result of selection effect. A few faint galaxies have ill-defined, low-S/N continuum which could produce

unusually large $[\text{O II}]$ equivalent widths (Fig. 4), but our measurement and associated uncertainty of equivalent widths via the flux-summing method (§ 2.2) generally is robust even with low-S/N spectra, i.e., it does not show a systematic bias toward larger equivalent widths unlike when a Gaussian is fitted to a low-S/N line profile. We checked the robustness by artificially degrading a high-S/N spectrum, with which a robust measurement of equivalent widths can be made, and actually measuring equivalent widths by the flux-summing method.

Although very strong $[\text{O II}]$ equivalent widths, e.g., $W([\text{O II}]) \lesssim -100 \text{ \AA}$, are generally observed with large uncertainties in faint galaxies below the survey completeness limit, the anti-correlation between the emission equivalent width and galaxy luminosity is clearly observed in $[\text{O II}]$ emission but appears almost non-existent in $\text{H}\alpha$ emission. At a glance, there is a strong suppression of emission equivalent widths in very luminous galaxies. In fact, some of the most luminous galaxies, i.e., $M_V < -22$, are classified as AGN-like, whereas few very luminous galaxies with high $[\text{O II}]$ emission equiv-

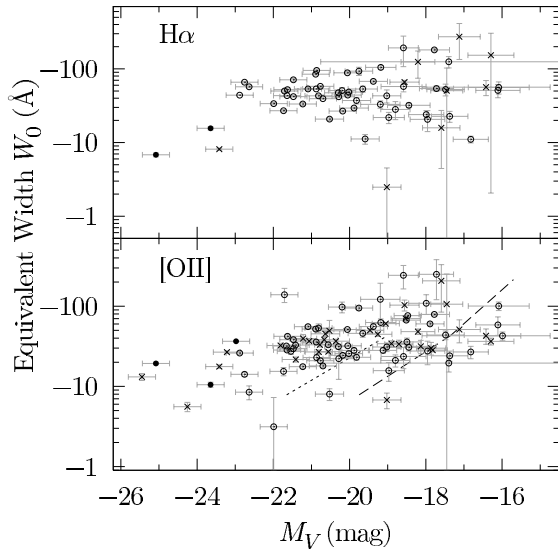


FIG. 7.— Rest-frame [O II] (*bottom*) and $H\alpha$ (*top*) equivalent width of the cluster [O II] emitters as a function of their absolute V magnitude. Symbols are as in Fig. 6. Dashed and dotted lines in the bottom plot roughly indicate the sensitivity limits of MLF00 narrowband survey for galaxies extending over $3''/8$ (9 pixels) and $1''/4$ (200 pixels), respectively. For some galaxies $H\alpha$ was outside the observed spectral range while their [O II] equivalent width could be measured.

alent width exist in the same luminosity range. That AGNs are preferentially hosted in very luminous objects is not surprising, but it is not clear that the absence of low-luminosity AGNs (i.e., $M_V > -22$) is real or is due to selection bias. It is known that the strength of [O II] and $H\alpha$ emission, when excited by AGNs, correlates tightly with the AGN luminosity. Therefore if the observed mean equivalent width of the luminous AGN-like galaxies, of order of $\sim 10 \text{ \AA}$, were to set roughly the maximum equivalent width, most AGNs of lower luminosity would be expected to drop out of our detection limit.

A potentially intriguing interpretation of Fig. 7 is a manifestation of so-called *downsizing effect*, which refers to observational evidence for the redshift evolution of characteristic galaxy luminosity above which star formation activities are suppressed (Cowie et al. 1996). Such characteristic luminosity at which the suppression of vigorously star-forming galaxies evolves toward less luminous end at lower redshifts. Now, AGN activity has been shown by simulations to be more effective in suppressing star formation in major galaxy mergers than those involving no nuclear activities (Springel et al. 2005). Visual inspection of our images indicates the AGN-like galaxies to be located in among the densest regions in terms of projected surface number density of galaxies. Our imaging does not have the resolution to clearly see the signature of mergers, yet the distribution of AGN-like galaxies in our sample might suggest the implicit role of AGN activities in regulating star formation activity in large galaxies. While the interpretation is highly speculative and there have been little direct observational support, recently a number of studies which provide circumstantial evidence in support for this scenario have been emerging. For example, the buildup of cluster red sequence appears to start from the high-luminosity end (De Lucia et al. 2004), while the number of post-starburst galaxies appear to host AGN activities (C. Tremonti et al. 2006, private communication). In view of these recent findings, the weaker [O II] equivalent widths found in high-luminosity AGN-like galaxies in our sample

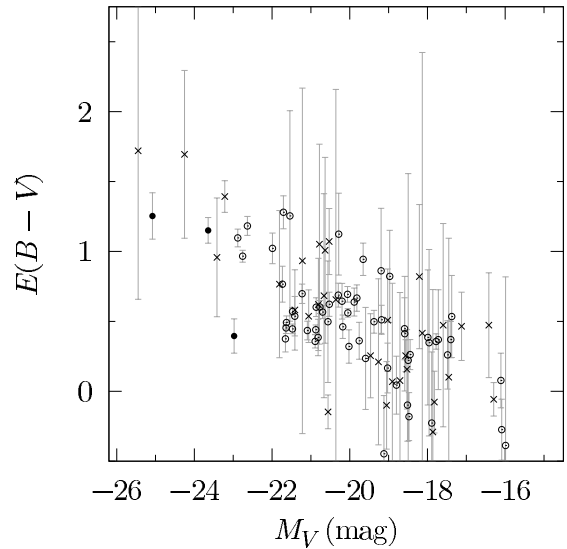


FIG. 8.— Reddening $E(B-V)$ of cluster [O II] emitters as a function of their absolute V magnitude. The symbols have the same meaning as in Fig. 6.

are at least consistent with AGNs suppressing cluster star-forming activities. We will revisit this argument by analyzing the star formation histories, local environments, and archival *HST* morphology of the cluster [O II] emitters in the forthcoming paper in the series.

Putting the high-luminosity [O II] emitters aside, interpreting such a luminosity trend as in Fig. 7 is not trivial, since both metallicity and the amount of dust extinction generally show a positive trend with galaxy luminosity (e.g., Heckman et al. 1998; Tremonti et al. 2004) and affect star formation diagnostics like emission equivalent width. In particular, Charlot et al. (2002) found in their sample of local galaxies drawn from the Stromlo-APM redshift survey that the star formation rate per unit luminosity showed little dependence on luminosity, when dust extinction was properly accounted for. We see an indication of significance of dust extinction when [O II] and $H\alpha$ emission equivalent widths are compared, i.e., [O II] equivalent widths show a stronger trend with luminosity than $H\alpha$ equivalent widths.

The equivalent width of nebular emission line such as [O II] and $H\alpha$ is essentially a ratio of the total emission flux from an ensemble of localized H II regions to the continuum emission from stellar population more widely distributed throughout a galaxy. It is empirically known that nebular emission lines suffer more dust extinction than the stellar continuum (Calzetti et al. 1994). Therefore dust extinction generally reduces the strength of emission equivalent width, and that effect is selectively stronger at shorter wavelengths, i.e., blue emission line suffers more from this effect due to the wavelength dependence of dust absorption. In Fig. 8 we see that the reddening $E(B-V)$ of cluster [O II] emitters shows a trend with their luminosity, especially at the most luminous end; the Jansen et al. sample showed a similar trend, although their galaxies were not as reddened as ours. Thus the observed trend of decreasing emission equivalent widths with galaxy luminosity in Fig. 7 could be enhanced by the greater amount of dust extinction in high luminosity galaxies. Furthermore, the positive luminosity trend of $E(B-V)$ points to the importance of metallicity in decoupling the [O II]/ $H\alpha$ ratio trend with luminosity and reddening (Fig. 6), since the dust abundance is expected to scale with metallicity, and the [O II]/ $H\alpha$ ratio of nearby galaxies has been shown to correlate nontriv-

ially with the metallicity as well as ionization state of emission nebula (Kewley et al. 2004; Mouhcine et al. 2005). With rather large uncertainties, we may not convincingly say if the low-luminosity galaxies in our sample are more reddened than the local counterparts. Yet a preliminary analysis of the H δ -strong galaxy fraction in our sample shows a higher incidence of dusty starburst galaxies in this cluster compared to a local field sample, probably due to galaxy-galaxy interactions. In a future paper we also wish to explore the metallicity effect on [O II]/H α .

5. SUMMARY

We have reported on a spectroscopic follow-up confirmation of faint [O II] emitters in Abell 851 catalogued by MLF00. The Keck I/LRIS and Keck II/DEIMOS spectra have confirmed [O II] λ 3727 emission lines of the narrowband-selected cluster [O II] emitters at a \approx 85% success rate for faint ($i \lesssim 25$) blue ($g-i < 1$) galaxies. The rate for the successful detection of [O II] emission is a strong function of galaxy color, generally proving the efficacy of narrowband technique supplemented with broadband colors in wide-field search for faint emission-line objects. Balmer decrement-derived reddening measurements show these galaxies are very dusty, with a significant fraction of the population showing $E(B-V) \gtrsim 0.5$. Even after correcting for dust extinction, the [O II]/H α ratio for very high $E(B-V)$ galaxies remains generally lower by a factor of ~ 2 than the mean [O II]/H α ratios reported by the studies of nearby galaxies. A slight luminosity trend of [O II]/H α can be mostly removed by reddening correction, yet the emission line flux ratio for high-

$E(B-V)$ galaxies remains much lower regardless of their luminosity. In a future paper, we will further test the metallicity dependence of [O II]/H α ratio, which the previous studies of nearby galaxies have shown to be strong. The luminosity trend of [O II] and H α emission equivalent width strength, coupled with the abundance of luminous AGN-like galaxies, is consistent with AGNs suppressing star-forming activities for massive cluster galaxies, although further studies specifically addressing this issue need to be carried out.

T.S. thanks Michael Cooper and Jeff Newman for assistance in the use of DEEP2 DEIMOS Data pipeline. T.S. also thanks Marcin Sawicki, Tommaso Treu, and Jong-Hak Woo for useful conversations. We thank an anonymous referee for valuable comments which improved the presentation of this paper. Financial support was provided by the David and Lucille Packard Foundation and the Alfred P. Sloan Foundation. This research has made use of the NASA/IPAC Extragalactic Database (NED), which is operated by the Jet Propulsion Laboratory, California Institute of Technology, under contract with the National Aeronautics and Space Administration. This research has made use of the NASA Astrophysics Data System abstract service. The authors wish to recognize and acknowledge the very significant cultural role and reverence that the summit of Mauna Kea has always had within the indigenous Hawaiian community. We are most fortunate to have the opportunity to conduct observations from this mountain.

Facilities: Keck:I (LRIS), Keck:II (DEIMOS)

REFERENCES

- Abraham, R. G., van den Bergh, S., Glazebrook, K., Ellis, R. S., Santiago, B. X., Surma, P., & Griffiths, R. E. 1996, *ApJS*, 107, 1
- Balogh, M. L., Morris, S. L., Yee, H. K. C., Carlberg, R. G., & Ellingson, E. 1997, *ApJ*, 488, L75
- Blanton, M., & Lin, H. 2000, *ApJ*, 543, L125
- Blanton, M. R., et al. 2003, *AJ*, 125, 2348
- Bruzual, G., & Charlot, S. 2003, *MNRAS*, 344, 1000
- Butcher, H., & Oemler, A. 1984, *ApJ*, 285, 426
- Calzetti, D., Kinney, A. L., & Storchi-Bergmann, T. 1994, *ApJ*, 429, 582
- Calzetti, D., Armus, L., Bohlin, R. C., Kinney, A. L., Koornneef, J., & Storchi-Bergmann, T. 2000, *ApJ*, 533, 682
- Charlot, S., Kauffmann, G., Longhetti, M., Tresse, L., White, S. D. M., Maddox, S. J., & Fall, S. M. 2002, *MNRAS*, 330, 876
- Cowie, L. L., Songaila, A., Hu, E. M., & Cohen, J. G. 1996, *AJ*, 112, 839
- De Filippis, E., Schindler, S., & Castillo-Morales, A. 2003, *A&A*, 404, 63
- De Lucia, G., et al. 2004, *ApJ*, 610, L77
- Dressler, A. 1980, *ApJ*, 236, 351
- Dressler, A., & Gunn, J. E. 1992, *ApJS*, 78, 1
- Dressler, A., Smail, I., Poggianti, B. M., Butcher, H., Couch, W. J., Ellis, R. S., & Oemler, A. J. 1999, *ApJS*, 122, 51
- Faber, S. M., et al. 2003, *Proc. SPIE*, 4841, 1657
- Gallagher, J. S., Hunter, D. A., & Bushouse, H. 1989, *AJ*, 97, 700
- Heckman, T. M., Robert, C., Leitherer, C., Garnett, D. R., & van der Rydt, F. 1998, *ApJ*, 503, 646
- Hicks, E. K. S., Malkan, M. A., Teplitz, H. I., McCarthy, P. J., & Yan, L. 2002, *ApJ*, 581, 205
- Ho, L. C. 1996, *ASP Conf. Ser.* 103: The Physics of Liners in View of Recent Observations, 103
- Hogg, D. W., Cohen, J. G., Blandford, R., & Pahre, M. A. 1998, *ApJ*, 504, 622
- Jansen, R. A., Franx, M., & Fabricant, D. 2001, *ApJ*, 551, 825
- Kauffmann, G., et al. 2003, *MNRAS*, 346, 1055
- Kauffmann, G. 1995a, *MNRAS*, 274, 153
- Kauffmann, G. 1995b, *MNRAS*, 274, 161
- Kennicutt, R. C. 1992, *ApJ*, 388, 310
- Kennicutt, R. C. 1998, *ARA&A*, 36, 189
- Kewley, L. J., Geller, M. J., & Jansen, R. A. 2004, *AJ*, 127, 2002
- Kewley, L. J., Dopita, M. A., Sutherland, R. S., Heisler, C. A., & Trevena, J. 2001, *ApJ*, 556, 121
- Kodama, T., Smail, I., Nakata, F., Okamura, S., & Bower, R. G. 2001, *ApJ*, 562, L9
- Kodama, T., et al. 2005, *PASJ*, 57, 309
- Le Floch, E., et al. 2005, *ApJ*, 632, 169
- Lilly, S. J., Le Fevre, O., Hammer, F., & Crampton, D. 1996, *ApJ*, 460, L1
- Lotz, J. M., Martin, C. L., & Ferguson, H. C. 2003, *ApJ*, 596, 143
- Madau, P., Ferguson, H. C., Dickinson, M. E., Giavalisco, M., Steidel, C. C., & Fruchter, A. 1996, *MNRAS*, 283, 1388
- Martin, C. L., Lotz, J., & Ferguson, H. C. 2000, *ApJ*, 543, 97 (MLF00)
- Massey, P., Strobel, K., Barnes, J. V., & Anderson, E. 1988, *ApJ*, 328, 315
- McCall, M. L., Rybski, P. M., & Shields, G. A. 1985, *ApJS*, 57, 1
- Moore, B., Lake, G., Quinn, T., & Stadel, J. 1999, *MNRAS*, 304, 465
- Moran, S. M., Ellis, R. S., Treu, T., Smail, I., Dressler, A., Coil, A. L., & Smith, G. P. 2005, *ApJ*, 634, 977
- Mouhcine, M., Lewis, I., Jones, B., Lamareille, F., Maddox, S. J., & Contini, T. 2005, *MNRAS*, 362, 1143
- Oke, J. B., et al. 1995, *PASP*, 107, 375
- Osterbrock, D. E. 1989, *Astrophysics of Gaseous Nebulae and Active Galactic Nuclei* (Mill Valley: Univ. Science Books)
- Schindler, S., Belloni, P., Ikebe, Y., Hattori, M., Wambsganss, J., & Tanaka, Y. 1998, *A&A*, 338, 843
- Schindler, S., & Wambsganss, J. 1996, *A&A*, 313, 113
- Schlegel, D. J., Finkbeiner, D. P., & Davis, M. 1998, *ApJ*, 500, 525
- Springel, V., Di Matteo, T., & Hernquist, L. 2005, *MNRAS*, 361, 776
- Tasitsiomi, A., Kravtsov, A. V., Gottlöber, S., & Klypin, A. A. 2004, *ApJ*, 607, 125
- Tremonti, C. A., et al. 2004, *ApJ*, 613, 898
- Treu, T., Ellis, R. S., Kneib, J. P., Dressler, A., Smail, I., Czoske, O., Oemler, A., & Natarajan, P. 2003, *ApJ*, 591, 53
- Zhao, D. H., Mo, H. J., Jing, Y. P., Börner, G. 2003, *MNRAS*, 339, 12